Peer-reviewed version available at *Crystals* **2019**, *9*, 643; doi:10.3390/cryst9120643

Article

A high-pressure investigation of the synthetic analogue of chalcomenite, $CuSeO_3 \cdot 2H_2O$

Javier Gonzalez-Platas[1,*], Placida Rodriguez-Hernandez[2], Alfonso Muñoz[2], U. R. Rodríguez-Mendoza[1], Gwilherm Nénert[3], and Daniel Errandonea[3,*]

[1]Departmento de Física, Instituto Universitario de Estudios Avanzados en Física Atómica, Molecular y Fotónica (IUDEA) and MALTA Consolider Team, Universidad de La Laguna, Avda. Astrofísico Fco. Sánchez s/n, E-38206 La Laguna, Tenerife, Spain; urguez@ull.edu.es (U.R.-M.)
[2]Departamento Física, Malta Consolider Team and Instituto de Materiales y Nanotecnología, Universidad de La Laguna, 38206 La Laguna, Tenerife, Spain; plrguez@ull.edu.es (P.R.-H.); amunoz@ull.edu.es (A.M.)
[3]Malvern Panalytical B.V., Lelyweg 1, 7602 EA Almelo, The Netherlands; gwilherm.nenert@malvernpanalytical.com (G.N.)
[4]Departamento de Física Aplicada - ICMUV - MALTA Consolider Team, Universitat de València, c/Dr. Moliner 50, 46100 Burjassot (Valencia), Spain
* Correspondence: jplatas@ull.edu.es (J.G.-P.) and daniel.errandonea@uv.es (D.E)

Abstract:

Synthetic chalcomenite-type cupric selenite $CuSeO_3 \cdot 2H_2O$ has been studied at room temperature under compression up to pressures of 8 GPa by means of single-crystal X-ray diffraction, Raman spectroscopy, and density-functional theory. According to X-ray diffraction, the orthorhombic phase undergoes an isostructural phase transition at 4.0(5) GPa with the thermodynamic character being first-order. This conclusion is supported by Raman spectroscopy studies which have detected the phase transition at 4.5(2) GPa and by the first-principles computing simulations. The structure solution at different pressures has provided information on the change with pressure of unit-cell parameters as well as on the bond and polyhedral compressibility. A Birch-Murnaghan equation of state has been fitted to the unit-cell volume data. We found that chalcomenite is highly compressible with a bulk modulus of 42 – 49 GPa. The possible mechanism driving changes in the crystal structure is discussed, being the behavior of $CuSeO_3 \cdot 2H_2O$ mainly dominated by the large compressibility of the coordination polyhedron of Cu. On top of that, an assignation of Raman modes is proposed based upon density-functional theory and the pressure dependence of Raman modes discussed. Finally, the pressure dependence of phonon frequencies is also reported.

Keywords: Cu(II); selenite; chalcomenite; crystal structure; x-ray diffraction; Raman spectroscopy; high pressure, equation of state, density functional theory

1. Introduction

Compounds containing divalent copper (Cu) have very interesting physical properties which are mainly related to the typical low-symmetry distortion around the Cu^{2+} ion [1]. On the other hand, selenite compounds are fascinating materials because they contain cations with lone pairs of electrons which give them particular characteristics [2]. Chalcomenite-type cupric selenite $CuSeO_3 \cdot 2H_2O$ matches these two conditions, being therefore a quite attractive compound. On top of that, it has the additional interest of containing water molecules [3] which is known to influence the chemical and physical properties of the material [4].

$CuSeO_3 \cdot 2H_2O$ has an orthorhombic crystal structure (space group $P2_12_12_1$) [5] which is shown in Fig. 1. It is formed by cross-linked chains of Cu and Se coordination polyhedra. The SeO_3 units alternate with CuO_5 group in square pyramidal coordination forming chains parallel to the *b*-axis.

Preprints (www.preprints.org) | NOT PEER-REVIEWED | Posted: 19 November 2019 doi:10.20944/preprints201911.0227.v1

Peer-reviewed version available at Crystals 2019, 9, 643; doi:10.3390/cryst9120643

The adjacent chains are connected by H atoms weakly bonded to O atoms. An empty cavity occurs in the structure which is related to the Se lone pair of electrons.

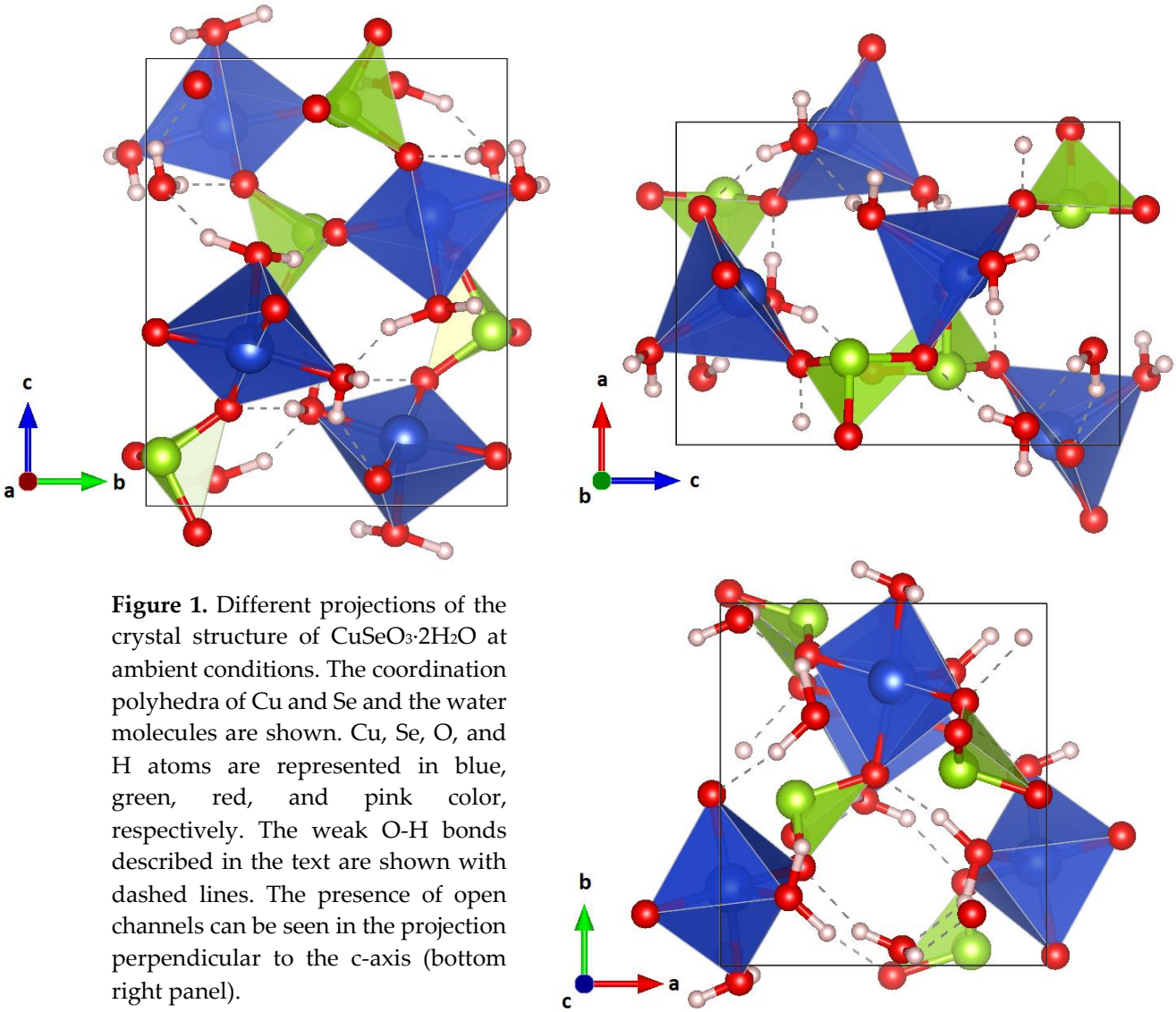

Figure 1. Different projections of the crystal structure of $CuSeO_3 \cdot 2H_2O$ at ambient conditions. The coordination polyhedra of Cu and Se and the water molecules are shown. Cu, Se, O, and H atoms are represented in blue, green, red, and pink color, respectively. The weak O-H bonds described in the text are shown with dashed lines. The presence of open channels can be seen in the projection perpendicular to the c-axis (bottom right panel).

After the accurate determination of the crystal structure, most studies of chalcomenite have been focused in its lattice vibrations [6, 7] and thermophysical and thermochemical properties [8, 9]. All these studies have been carried out at ambient pressure. However, it is known that high pressure (HP) could lead to interesting phenomena in minerals, including pressure-driven phase transitions [10]. In particular, HP studies have been performed in hydrated minerals related to chalcomenite, like $FeSO_4 \cdot H_2O$ and $MgSO_4 \cdot H_2O$, leading to results relevant for Earth and Planetary Sciences [11, 12]. However, nothing is known of the effects of HP in chalcomenite.

We report here a systematic study of the HP behavior of $CuSeO_3 \cdot 2H_2O$ up to 8 GPa. The effects of pressure on the crystal structure and phonons have been studied by a combination of single-crystal X-ray diffraction (SC-XRD) and Raman experiments with density-functional theory (DFT) calculations. Such approach has proven to be successful or understanding the HP behavior of oxides [13]. In the present case, we have found evidences of the existence of a first-order isostructural phase transition and determined the influence of pressure on crystal-structure parameters and phonon frequencies. The changes observed have been related to modifications induced by pressure in the different polyhedral units.

2. Materials and Methods

2.1 Sample preparation

A stock solution of $Cu(NO_3)_2{\cdot}3H_2O$ with a concentration of 1 mole per liter was prepared in water. A second stock solution of SeO_2 dissolved in water was prepared separately with also a 1 mole/liter concentration. An agar gel of 1.5% in weight was prepared containing $Cu(NO_3)_2{\cdot}3H_2O$ solution. Prior to the gel formation, the pH of the solution was adjusted to pH = 2 using concentrated HNO_3 acid. Once the gel was settled, 5mL of the SeO_2 stock solution was poured on top of the gel for diffusion. After few days, single crystals of $CuSeO_3{\cdot}2H_2O$ started to appear and were handpicked for single crystal diffraction experiment. The nature and the purity of the as-grown was confirmed by the Rietveld refinement of a powder x-ray diffraction. The data were collected at room temperature (and pressure) on a fine powder obtained from crushed single crystals using a Cu K_α wavelength. The collected pattern of the as-synthetized sample and the corresponding Rietveld refinement are shown in Fig. 2 together with the residuals. The refinement was carried out using the HighScore suite [14]. All the observed peaks can be accounted by the known crystal structure [5], which leads to small residuals. The resulting cell parameters were a = 6.6719(2) Å, b = 7.3710(2) Å, and c = 9.1718(2) Å.

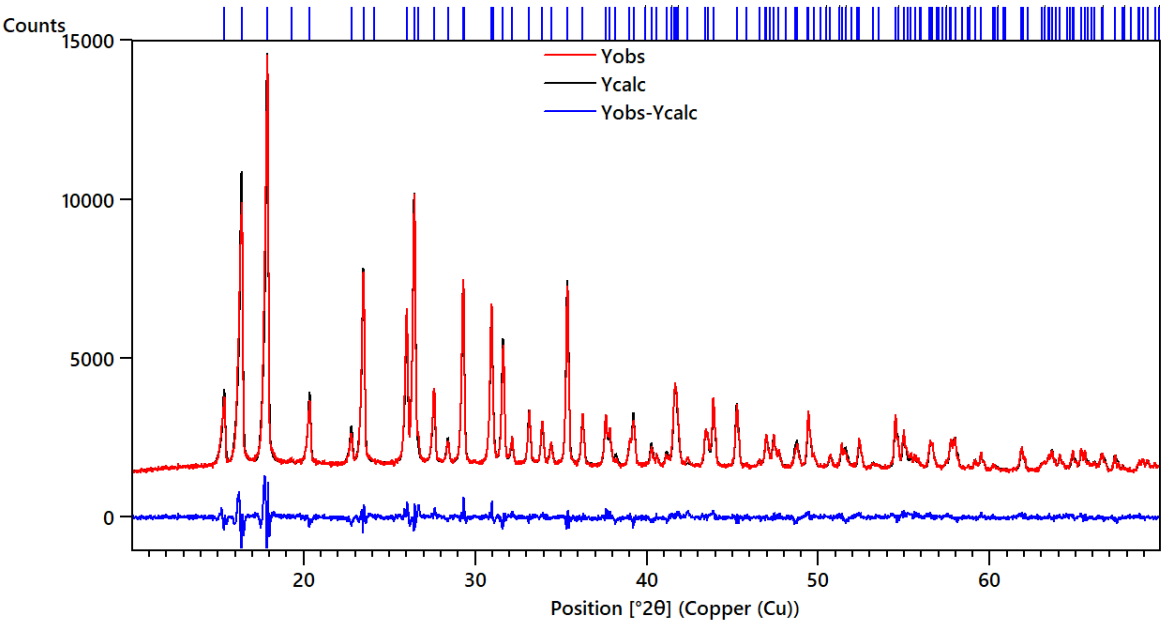

Figure 2. Powder x-ray diffraction pattern of synthetic chalcomenite collected at room conditions (black). The refinement is shown in red and the residuals in blue. Ticks indicate the positions of Bragg peaks.

2.2 Experimental details

All SC-XRD measurements were made at room temperature using an Agilent SuperNOVA diffractometer equipped with an EOS detector (CCD) and Mo K_α radiation micro-source. All measurements were processed with the CrysAlisPro software [15]. Numerical absorption correction based on gaussian integration over a multifaceted crystal model was applied using the ABSORB program [16]. For high-pressure measurements, we have employed a Mini-Bragg diamond anvil cell (DAC) from Almax-EasyLab, with an opening angle of 90º and equipped with anvil culets of 500 µm diameter, fitted with a stainless gasket pre-indented to a 75 µm thickness, and containing a centered hole of 200 µm diameter. A methanol-ethanol mixture (4:1) was used as pressure-transmitting medium, which remains hydrostatic in the range of pressure used in our experiments [17]. The sample was placed on one of the diamonds anvils (diffracted side) together with a small ruby sphere used as pressure sensor [18]. Pressure was determined with an accuracy of 0.04 GPa. Special attention was taken to avoid sample bridging between the two diamond anvils [19].

The crystal structure was refined, for each pressure, using previous results as starting point, on F^2 by full-matrix least-squares refinement with the SHELXL program [20]. Due to limitations of the opening angle of our DAC, it is only possible to collect about 60-70% of the reflections present in a full dataset at ambient conditions. In general, the atoms were refined anisotropically, with the exception of some oxygen atoms because in some cases it was only possible to do it in isotropic thermal parameters. No restraints were used during this process.

Raman experiments were performed with the same DAC setup used in the SC-XRD experiments and the same pressure medium and scale. Raman spectra were acquired employing a commercial scanning confocal Raman instrument (Renishaw InVia) exciting with a continuous-wave operation diode laser at 532 nm and detecting with a thermo-electric cooled CCD detector achieving a spectral resolution of 0.5 cm^{-1} with an 1800 l/mm grating. A 20x long working distance objective was used to achieve on the sample a laser-spot diameter of less than 5 μm. The laser power on the sample was smaller than 20 mW.

2.3 Density-functional theory calculations

We have performed DFT *ab initio* total-energy simulations of the properties of chalcomenite. The Vienna ab initio simulation package (VASP) [21] was employed with the projector-augmented wave pseudopotential and the plane-wave method [22]. The exchange-correlation energy was described by the generalized-gradient approximation with the Perdew-Burke-Ernzerhof for solids (PBEsol) prescription [23]. Van der Waals interaction were not included in these calculations. For comparison, we also carried out simulations using PBE pseudopotentials and including Van der Waals interactions [24]. In both type of computational simulations, plane wave kinetic energy cutoffs of 530 eV and dense meshes of special k-points generated with the Monkhorst-Pack scheme [25] were employed. For the considered structure, full optimizations of all the structural parameters were performed at different selected volumes. In the final optimized configurations, the atomic forces on the atoms were lower than 0.005 eV/Å, and the differences between diagonal components of the stress tensor less than 0.1 GPa. The equation of state was derived from the energy-pressure-volume (E, V, P) data obtained at each of the selected volumes [26]. Temperature and zero-point motion effects were not included in the present simulations.

Lattice vibrations were simulated to study the phonons at the zone center (Γ point) of the Brillouin zone with the direct force-constant approach [27]. The symmetry, polarization vectors, and phonon frequencies as well as the irreducible representation and the character of all the phonons of chalcomenite at Γ were provided by the diagonalization of the dynamical matrix. We have performed accurate calculations of the forces on the atoms when fixed small displacements from the equilibrium configuration are considered, to obtain this dynamical matrix. The crystal symmetry was used to reduce the number of independent displacements needed.

3. Results and discussion

3.1 Structural analysis

Our SC-XRD experiments at ambient conditions confirmed that $CuSeO_3 \cdot 2H_2O$ crystallizes in the orthorhombic space group $P2_12_12_1$ (Nº. 19). The determined unit-cell parmeters agree well with those we determined from powder XRD. As described by Robinson *et al.* [5] and shown in Fig. 1, the structure is composed of chain containing polyhedra with Cu in square pyramidal coordination alternating with SeO_3 units. Within each chain all the Cu pyramids point in the same general direction. In addition, every chain is surrounded by four chains with Cu pyramids oriented in the opposite direction. The results of the experiment made at ambient conditions, which served as reference for HP experiments, are summarized in Table 1.

Table 1. Crystal data and structure refinement parameters for $CuSeO_3 \cdot 2H_2O$ at ambient conditions.

Formula	CuH_4O_5Se
D_{calc} (g cm^{-3})	3.341
μ (mm^{-1})	12.840
Formula Weight	226.53
Size (mm^3)	0.10×0.08×0.03
Crystal System	orthorhombic
Space Group	$P2_12_12_1$
a (Å)	6.6720(2)
b (Å)	7.3669(2)
c (Å)	9.1613(3)
α (º)	90
β (º)	90
γ (º)	90
V (Å^3)	450.30(2)
Z	4
Wavelength (Å)	0.71073
$\Theta_{min}/\Theta_{max}$ (º)	3.549/29.817
Reflections (collected/unique)/R_{int}	1441/1058/0.0126
Parameters/Restraints	66/0
Largest Peak/Deepest Hole (e/Å^3)	0.747/-0.761
GOF	1.132
wR_2/R_1	0.0633/0.0247

From experiments under HP conditions, we have obtained the pressure dependence of unit-cell parameters. On Fig. 3 we show our experimental results (from two independent experiments) together with the results from our computer simulations. From the calculations we found that the inclusion of weak van der Waals interactions leads to a less accurate description of the unit-cell volume at ambient pressure. In particular, it is underestimated by 3%. In addition, calculations neglecting these interactions provide a better description of the effects of pressure in the crystal structure. This can be seen in Fig. 3. The calculations not considering the van der Waals interactions are those shown in solid blue symbols (while those including these interactions are the empty blue symbols). They are the ones that better agree with our experiments. All these facts suggest that van der Waals interactions are not accurately described in computing simulations [28] of the HP behavior of chalcomenite.

For the pressure-dependence of the *c*-axis we observe a nearly linear pressure evolution, with experiments and calculations in qualitative agreement. For the *a*- and *b*-axis a non-linear pressure dependence has been found. In particular, in the *a*-axis, there is a slope change observed at a critical pressure of around 3.5 GPa in run 1 and at 4 GPa in the second experiment. This fact is highlighted by solid lines in Fig. 3, which represent the pressure dependence in the *a*-axis below and above the critical pressure. Calculations show a slightly different pressure behavior of the *a*-axis, but also found a kink at 4 GPa. On the other hand, in the *b*-axis we found a decrease with pressure up to 4.4 GPa where a minimum value is reached, and beyond this pressure this unit-cell parameter increases with pressure. Again, calculations shown a qualitative similar behavior, but with the minimum close to 8 GPa. The above described changes are typical of pressure-driven isostructural phase transitions [29]. Since changes were observed at 3.5 and 4.4 GPa in the different axes, we estimate the transition pressure to be 4.0(5) GPa. Interestingly the transition will cause a collapse of the empty cavities

present in the structure of chalcomenite (See Fig. 1). This collapse will favor a faster decrease of the *a*-axis after the transition and the expansion of the *b*-axis, as we found in our experiments.

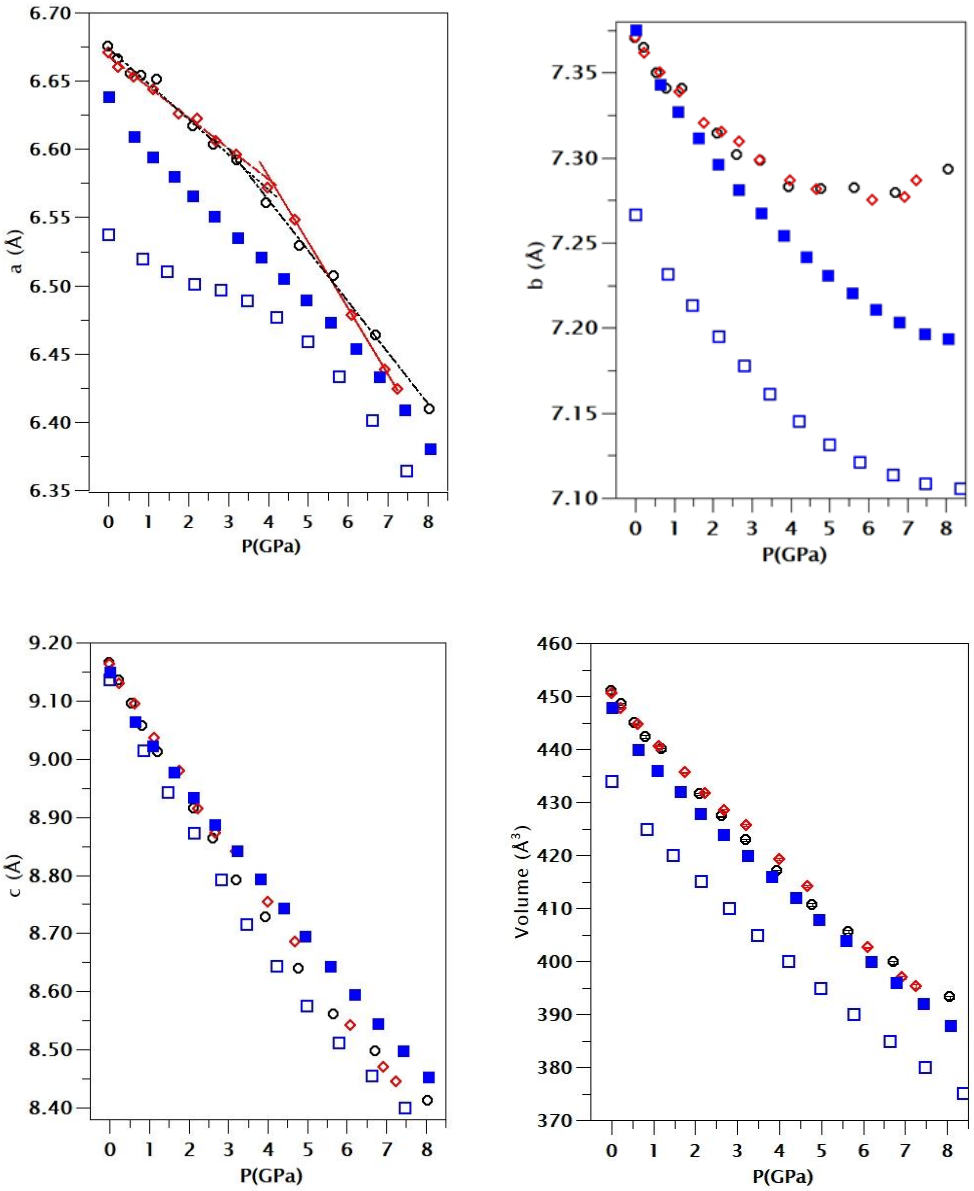

Figure 3. Pressure dependence of unit-cell parameters and volume of $CuSeO_3 \cdot 2H_2O$. Error bars are comparable to symbols sizes. Black and red symbols are from different experiments (run 1 and 2, respectively). Solid blue squares are from PBEsol calculations (without van der Waals interactions) and empty blue squares are from calculations including van der Waals interactions. In the plot of the *a*-axis we have included solid lines to highlight the slope change of the pressure dependence observed around 3.5 GPa in run 1 and 4 GPa in run 2.

The existence of a phase transition is confirmed by Raman experiments (to be discussed below) which found evidence of the transition at 5.2(2) GPa. The proposed transition is isostructural since at all pressure XRD diffraction patterns can be identified with the space group $P2_12_12_1$. The phase transition could be characterized as a second-order transition [30], because the pressure evolution of unit-cell parameters is continuous but there is a discontinuity in the compressibility. However, as we will discuss next, discontinuous changes observed in bond distances indicate that the observed isostructural transition is a first-order transition. Interestingly, the change in the pressure dependency of unit-cell parameters does not affect the volume compressibility as can be seen in Fig.

3. This behavior resembles the HP behavior of related hydrated minerals, like $FeSO_4 \cdot H_2O$ and $MgSO_4 \cdot H_2O$ [11, 12], which also undergo phase transitions at similar pressures.

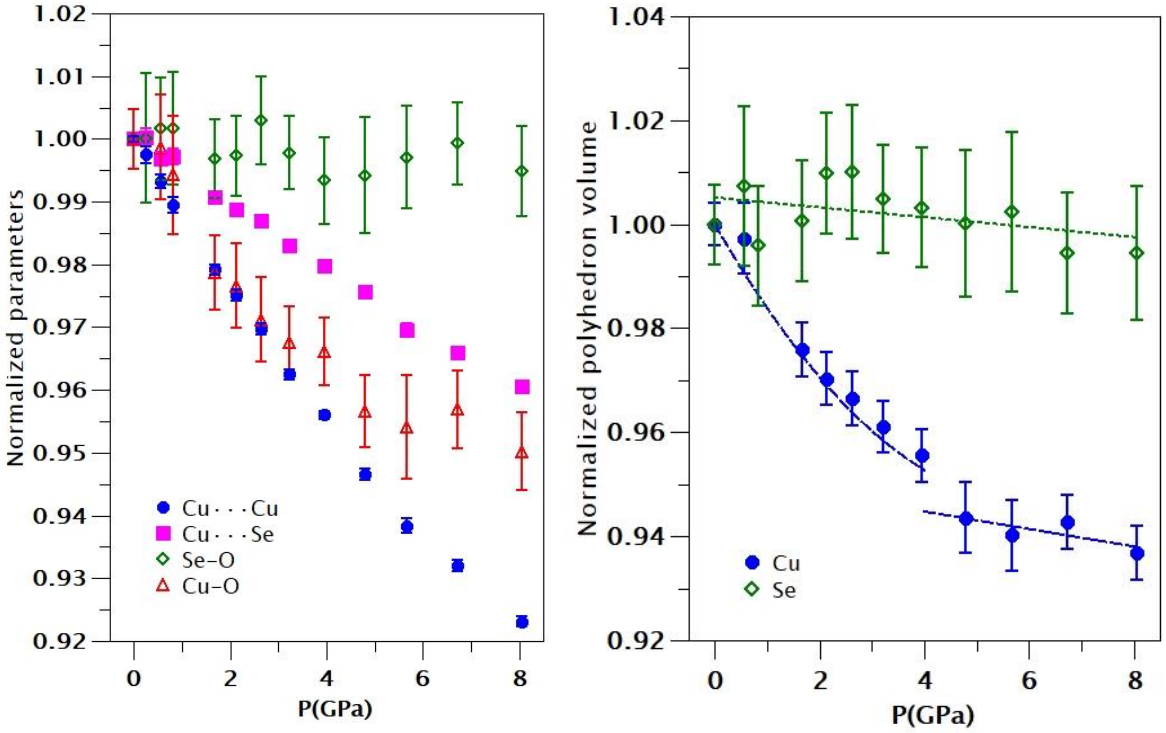

Figure 4. (Left) Pressure dependence of Cu···Cu, Cu-···Se, Se-O, and Cu-O interatomic distances. Error bars for Cu···Cu and Cu-···Se distances are smaller than the symbols. (Right) Pressure dependence of the SeO_3 and CuO_5 polyhedra.

In order to understand the changes that occur in the crystal structure at the phase transition we have analyzed what happen with the different polyhedral units. Geometrics dependences with pressure have been calculated from run 1. Results from the second run are similar. The results are shown in Fig. 4. From these results we can conclude some general aspects: 1) The triangular pyramid SeO_3 is more rigid than the squared pyramid CuO_5. This conclusion is consistent with the HP behavior of different selenates [31, 32]. As a consequence, the HP behavior of CuO_5 will dominate the axial and volume compressibility of the studied compound. 2) The compression of the CuO_5 polyhedron undergoes a sudden decrease at 4 GPa, which is the transition pressure. This indicates that the transition is related to a reorganization of oxygen atoms around Cu. In fact, we have notice that under compression there is a sixth oxygen atom, with a Cu-O distance of 3.15 Å at ambient pressure, which rapidly approaches Cu under compression. Beyond the transition pressure, it can consider that Cu is not anymore five coordinated but 5+1 coordinated. 3) Cu···Cu distances decreases around 8% (along *c*-axis) and most of the hydrogen bonds have directions parallel to *a*- and *b*-axis. We consider that H···H interactions could be in part responsible of the observed phase transition. Below 4 GPa, there is a H···H bond distance, with is mainly orientated along the *b*-axis, decreasing very rapid with pressure. The distance is between two hydrogens which belong to different H_2O molecules connected one to Cu and the other to Se. At ambient pressure there is an empty cavity in between these two hydrogens (as we described before). However, as under compression the H···H distance becomes considerably shorter at some point (transition pressure) the electrostatic repulsion between hydrogens make that the H···H distance stops decreasing, impeding the compression along the *b*-axis (in fact the expansion of this axis is favored). The presence of this new H···H bond will make the crystal to prefer to compress along *a*-axis instead of *b*-axis (as below the transition pressure) changing the compressibility of both axes and favoring the structural reorganization associated to the phase transition of $CuSeO_3 \cdot 2H_2O$. In summary, all the evidence described above points towards a

purely displacive transitions, where the SeO_3 groups remains unchanged in their topology, and the formation of additional Cu-O and H···H interactions modify the mechanical properties of chalcomenite. This transformation mechanism should be confirmed by future studies. In particular, HP neutron studies in deuterated samples could be very useful for studying hydrogen bonds.

3.2 Equation of states

We have analyzed the results obtained for the pressure dependence of the volume employing a Birch-Murnaghan equation of state (EOS) [33] using the EoSFit software [34]. The results are shown in Fig. 5. We have found that for run 2 our results can be properly described by a third-order EOS. We got V_0 = 451.0(3) Å^3, K_0 = 42(1) GPa, and K_0' = 4.6(4). For run 1 we found that a fourth-order EOS is needed. We got V_0 = 450.54(5) Å^3, K_0 = 49(2) GPa, K_0' = 5(2), and K_0'' = -1.4(9). From DFT calculations we got V_0 = 436.7 Å^3, K_0 = 49.3 GPa, and K_0' = 2.6 when van der Waals interactions are included and V_0 = 450.4 Å^3, K_0 = 50.0 GPa, and K_0' = 2.2 when they are not included. All the results for the bulk modulus agree within 10% showing that chalcomenite is highly compressible. Calculations tends to slightly overestimate K_0 and underestimate K_0'.

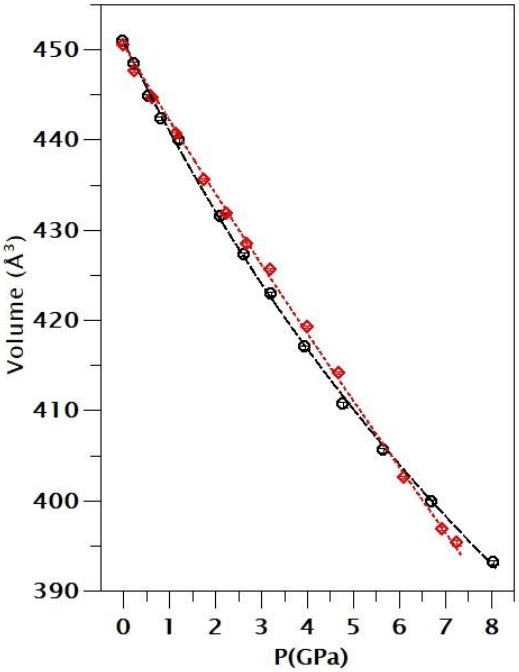

Figure 5. EOS fit of the pressure-volume results of the two runs. Black: run 1. Red: run 2. The solid lines are the fits and the symbols the experimental results.

We will compare now the compressibility of chalcomenite with related hydrated oxides. The obtained bulk modulus is similar to that of $FeSO_4·H_2O$ (45 GPa) [12], $MgSO_4·9H_2O$ (50 GPa) [35], and $CaSO_4·2H_2O$ (44 GPa) [36]. It is known that hydrated oxides are more compressible than their dehydrated counterparts [37]. In particular, the presence of H_2O could dramatically influence the properties of minerals related to chalcomenite [38]. Two examples of it are Gypsum ($CaSO_4·2H_2O$, K_0 = 44 GPa) [36], with a bulk modulus which is around 70% the bulk modulus of anhydrite ($CaSO_4$, K_0 = 64 GPa) [39], and $MgSO_4$ hydrate (K_0 = 50 GPa), with a bulk modulus which is around 80% the bulk modulus of $MgSO_4$ (K_0 = 62 GPa) [40]. Thus, our study on $CuSeO_3·2H_2O$ is putting a constrain to the bulk modulus of $CuSeO_3$, which has not been experimentally studied yet. This parameter should be larger than 42 GPa (our lowest limit value). This suggests that the bulk modulus of 37 GPa obtained for CaSeO3, via DFT calculations, and reported in the Materials Project Website [41], is probably underestimated. On the other hand, the comparison of the present results with the bulk modulus of other hydrated oxides suggest that related compounds to chalcomenite like

$CuTeO_3 \cdot 2H_2O$ [42] and $ZnSeO_3 \cdot 2H_2O$ [43] are expected to have a similar bulk modulus in the range of 40-50 GPa.

3.3 Raman spectroscopy

Group theory classifies the lattice vibrations of chalcomenite as follows: $\Gamma = 33A + 33B_1 + 33B_2 + 33B_3$. One B_1, one B_2, and one B_3 modes are the acoustic modes. The rest 129 modes are Raman active, with the B modes being also infrared active. Out of these modes, a total of twenty-one Raman modes have been measured in different samples of synthetic and natural chalcomenite [7] for frequencies smaller than 1000 cm^{-1}. In addition, three broad bands have been measured above 2900 cm^{-1} [7]. The low-frequency modes can be assigned to internal vibrations of the SeO_3 and CuO_5 polyhedra. The high-frequency modes correspond to water vibrations [7]. Our calculations confirm this interpretation. They have been performed without including van de Walls interaction because this method gives a more accurate description of the pressure dependence of the unit-cell volume as discussed previously. In addition, the calculations show that bending and stretching vibrations of SeO_3 are mostly at frequencies larger than 600 cm^{-1} while CuO_5 vibrations are at lower frequencies. This is because the force constant associated to Se-O vibrations is smaller than the force constant of Cu-O vibrations since Se-O bonds (1.703 Å in average) are shorter than Cu-O bonds (2.035 Å in average).

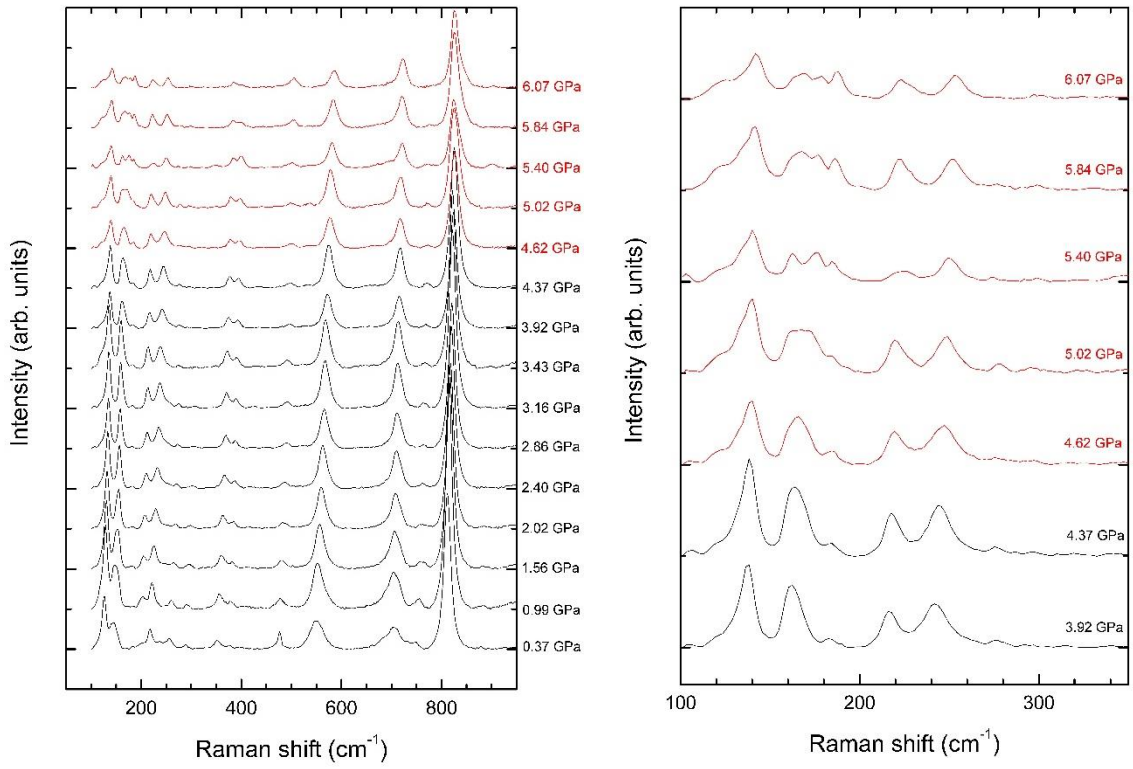

Figure 6. (Left) Raman spectra of chalcomenite measured at different pressures. (Right) Zoom of the low-frequency region to facilitate the identification of pressure-induced changes above 4.37 GPa. Pressure are indicated in the figure.

In our HP experiments, we have been focused in the low-frequency region which provide more information on the structural transition we have observed by XRD. In Fig. 6 we show Raman spectra measured under compression up to approximately 6.1 GPa. At low pressure we have observed twenty-two modes. They agree well with previous reported frequencies from different samples [7]. They also agree with our calculated frequencies, which are also in agreement with infrared experiments [44, 45]. A comparison of experiments and theory can be seen in Table 2 where all measured and calculated mode frequencies are reported. Calculations have been used for mode

assignment. Notice that according to calculations sixteen modes are predicted to have frequencies higher than 2680 cm^{-1} and other sixteen are predicted to be in the 1000 – 1625 cm^{-1} frequency region. This region has never been experimentally explored; thus our calculations provide information useful for future studies. We and the previous study [7] only see part of the remaining ninety-seven modes predicted for frequencies smaller than 1000 cm^{-1}. This is because some modes are very weak and many of them overlap in frequency (See Calculations in Table 2).

If attention is paid to the low-frequency part of the spectra in Fig. 6, it can be seen that there are changes in the Raman spectrum from 4.37 to 4.62 GPa which clearly show the occurrence phase transition. The main changes are the splitting of modes and changes in the intensity of some modes. The changes are more noticeable in the low-frequency region ($\omega < 300$ cm^{-1}), which is zoom in the right panel of Fig. 6. The observed changes are consistent with the changes we observed in the CuO_5 polyhedron and its gradual transformation into a CuO_6 polyhedron. Regarding the pressure evolution of modes, it is strongly non-linear as a consequence of the changes of the compressibility already described. An evidence of it is the fact that the modes follow a quadratic pressure dependence and many of them have a negative quadratic coefficient (See Table 2). In addition, modes with similar frequencies have in many cases very different pressure dependences as can be seen in Table 2. This favors the splitting of modes we have observed in the experiments. Analytical expressions describing the pressure dependence of Raman frequencies are given in Table 2. We have found that all Raman modes with $\omega < 1000$ cm^{-1} harden under compression. There is slight tendency of calculations for overestimating the pressure coefficient, but the agreement with experiments is still good. Regarding the high-frequency modes ($\omega > 1000$ cm^{-1}), calculations also predict a non-linear behavior, which indicates changes in the hydrogen bonding as concluded form XRD experiments. In addition, there are many high-frequency modes which soften under compression. The presence of such modes is usually associated to the existence of an instability that tends to make the crystal structure unstable [46, 47]. This fact is consistent with the finding of a displacive phase transition in our XRD experiments. The fact that there is no detectable volume change at the transition suggests the transition can be second-order, but the fact that there are discontinuities in bond distances supports a first-order transition.

Table 2. Experimental and theoretical Raman frequencies at ambient pressure (ω_0). The pressure dependence is described by a quadratic function: $\omega(P) = \omega_0 + \alpha_1 P + \alpha_1 P^2$ where P is in GPa. The parameters α_1 and α_2 are included in the table. Results from the literature are taken from the work by Frost *et al.* [7].

Mode	Literature	Present experiment			Calculations		
	ω_0 (cm^{-1})	ω_0 (cm^{-1})	α_1 (cm^{-1}/GPa)	α_2 (cm^{-1}/GPa^2)	ω_0 (cm^{-1})	α_1 (cm^{-1}/GPa)	α_2 (cm^{-1}/GPa^2)
A					67.9	2.72	0.06
B_2					75.0	0.77	-0.01
A					79.2	0.13	0.19
B_3					88.4	1.13	0.10
B_2					96.6	1.05	0.01
B_1					98.8	1.38	-0.03
B_3					110.4	2.93	-0.03
A					110.7	0.22	-0.07
B_1					111.1	0.44	0.01
B_1					115.8	3.27	-0.14
B_2					118.5	1.28	0.02
B_2					124.0	1.31	0.23
B_3	128-129	127	2.01	0.03	130.5	2.21	-0.06
A					134.2	1.43	-0.06
B_3					135.6	2.91	-0.08
B_1					136.5	4.71	-0.19
A	141-142	142	3.04	-0.02	138.9	3.13	-0.16
A					150.0	6.33	-0.38

B_3					151.0	1.92	0.03
B_2					152.0	6.51	-0.39
B_3					155.2	6.30	-0.15
B_2					165.3	4.48	-0.24
B_1		168	2.05	-0.05	169.0	2.16	-0.10
B_2					169.2	6.34	0.13
A					172.3	2.98	0.12
B_1	180	180	4.78	-0.05	178.2	5.43	-0.29
B_3					190.0	2.83	-0.06
B_1					194.9	1.39	0.17
A					195.5	2.57	0.03
B_3		198	5.50	0.00	197.6	6.01	-0.04
B_1					213.5	3.64	-0.09
A	218-219	218	4.78	-0.05	215.0	5.46	-0.16
B_1					220.8	2.09	0.26
B_2					227.0	4.00	-0.07
A					229.5	1.03	0.37
B_3					234.1	1.86	0.14
B_3					235.5	12.7	- 0.37
B_2		238	2.73	0.00	238.4	2.85	-0.01
B_1					241.1	13.4	- 0.56
A					244.2	11.8	- 0.49
B_2					247.6	12.7	-0.71
A	260	260	5.70	-0.02	269.0	6.81	-0.08
B_1					281.2	3.92	0.09
B_2					285.2	3.20	0.25
B_3		291	3.75	0.00	293.7	4.25	-0.06
B_2					300.7	9.77	-0.31
A					305.3	5.88	- 0.16
B_3					305.7	10.8	-0.43
B_1					306.4	10.1	-0.29
A					315.1	9.10	-0.20
B_3					337.3	7.11	-0.17
B_2	349	349	7.37	-0.11	337.4	9.46	-0.24
B_1					348.2	7.91	-0.15
B_3	361	361	8.80	-0.25	362.9	10.3	-0.31
A	367				365.0	8.60	-0.19
B_2	378	376	6.50	-0.11	374.6	6.72	-0.16
B_1	396-400	400	6.45	-0.13	398.4	6.84	-0.17
B_1					409.9	11.3	-0.39
B_3					423.7	10.1	-0.26
B_2					444.7	14.7	-0.69
A					454.7	11.9	-0.49
B_1					460.4	13.3	-0.34
B_2		465	8.75	-0.17	465.8	10.5	-0.24
A	472-476	475	8.88	-0.19	468.1	9.94	-0.22
B_3	489				481.3	14.2	-0.66
B_2					500.0	4.56	0.16
B_1					516.3	6.42	-0.02
B_3					516.5	4.68	0.11
A	550-552	549	7.57	0.00	518.8	8.79	-0.07
A					604.5	12.5	-0.74
B_3					608.7	5.92	-0.12

B_1					608.9	9.49	-0.47
B_2					624.8	5.70	-0.33
B_2					628.0	10.3	-0.61
B_3					632.5	11.8	-0.71
B_1					632.8	9.54	-0.47
A					634.5	4.50	-0.06
B_2					645.6	4.94	0.29
B_1					650.8	5.03	0.25
A					660.3	4.77	0.16
B_3	685-690	679	1.33	0.37	664.6	1.65	0.44
B_1	700-710	707	12.5	-0.88	716.4	17.6	-1.18
A	720				720.5	14.4	-0.94
B_3	727	729	11.9	-0.55	727.6	13.5	-0.84
B_2					735.1	14.8	-0.93
A					740.5	16.5	-0.78
B_1	749	748	15.5	-0.43	745.2	16.6	-0.56
B_3					751.5	16.3	-0.88
B_2					753.8	18.8	-0.86
B_3	792				809.7	10.6	-0.07
A	811-817	811	8.78	-0.05	814	10.4	-0.15
B_2					816.9	12.8	-0.38
B_1					828.7	9.36	-0.16
A					832.6	17.6	-0.10
B_3					839.7	18.1	-0.19
B_2					845.9	12.5	0.26
B_1		880	13.5	-0.11	848.2	16.6	-0.12
B_2	967				1023	11.3	-0.65
B_1					1026	11.7	-0.66
B_3					1030	14.6	-0.79
A					1031	13.8	-0.73
A					1051	18.9	-0.34
B_1					1054	20.3	-0.47
B_2					1054	20.1	-0.46
B_3					1056	17.6	-0.26
B_2					1560	-0.95	0.01
B_1					1564	-0.69	0.00
A					1580	-0.68	-0.03
B_3					1581	-0.27	-0.03
B_3					1601	1.64	-0.18
B_2					1604	2.55	-0.21
A					1624	-1.78	-0.07
B_1					1625	-1.68	-0.07
A					2685	-44.7	1.18
B_2					2688	-44.1	1.15
B_3					2700	-40.7	0.93
B_1					2709	-37.0	0.72
B_2					2766	-41.6	1.74
B_3					2771	-43.7	1.87
B_1					2773	-45.5	2.03
A	2909				2779	-40.4	1.63
A					3133	-26.7	-1.22
B_1					3136	-26.2	-1.23
B_3					3138	-26.5	-1.21

B_2	3193	3141	-26.6	-1.19
B_1		3357	-40.0	0.96
A		3360	-39.5	1.00
B_2		3362	-39.0	0.91
B_3	3507	3368	-38.8	0.97

4. Conclusions

By means of HP single-crystal XRD and Raman spectroscopy combined with DFT calculations, we have explored the HP behavior of synthetic chalcomenite $CuSeO_3 \cdot 2H_2O$ up to 8 GPa. We have found evidence for an isostructural phase transition at 4.0(5) GPa by XRD and at 4.5(2) GPa by Raman spectroscopy. We have also determined the polyhedral and volume compressibility. In particular, the P-V equation of state has been determined at room temperature. In addition, we have found that the HP behavior is governed by the compressibility and pressure induced changes in the coordination polyhedron of Cu. We also propose that H···H interactions could play a role in the observed phase transition. The reported transition is related to changes in the coordination polyhedron of Cu. These alterations induce notable modifications in the low-frequency Raman active modes. DFT calculations have helped for the assignment of Raman modes and provide information on modes not yet observed experimentally.

Author Contributions: Conceptualization, J.G.-P. and D.E.; XRD experiments, J.G.-P.; Raman experiments, U.R.R.-M. Sample preparation, G.N.; Formal analysis, J.G.-P. and D.E.; Computer simulations: P.R.-H. and A.M.; Writing—Review and Editing, all the authors.

Funding: This work was supported by the Spanish Ministry of Science, Innovation and Universities under grant MAT2016-75586-C4-1/3/4-P and by Generalitat Valenciana under grant Prometeo/2018/123 (EFIMAT).

Conflicts of Interest: The authors declare no conflict of interest.

References

1. J. Ruiz-Fuertes, A. Segura, F. Rodrıguez, D. Errandonea, and M. N. Sanz-Ortiz, Anomalous high-pressure Jahn-Teller behavior in $CuWO_4$, *Phys. Rev. Let.* **108** (2012) 166402.
2. L. Eklund and I. Persson, Structure and hydrogen bonding of the hydrated selenite and selenate ions in aqueous solution, *Dalton Trans.* **43** (2014) 6315 - 6321.
3. V. Vchirawongkwin, B. M. Rode and I. Persson, Structure and dynamics of sulfate ion in aqueous solution: An ab initio QMCF MD simulation and large angle X-ray scattering study, *J. Phys. Chem. B* **111** (2007) 4150–4155.
4. E. Bandiello, D. Errandonea, S. Ferrari, J. Pellicer-Porres, D. Martínez-García, S. N. Achary, A. K. Tyagi, and C. Popescu, Pressure-induced hexagonal to monoclinic phase transition of partially hydrated $CePO_4$, *Inorg. Chem.* **58** (2019) 4480-4490.
5. P. D. Robinson, P. K. S. Gupta, S. H. Swihart, and L. Houk, Crystal structure, H positions, and the Se lone pair of synthetic chalcomenite, $Cu(H_2O)_2[SeO_3]$, *American Mineralogist* **77** (1992) 834-838.
6. V. N. Bocharov, M. V. Charykova, and V. G. Krivovichev, Raman spectroscopic characterization of the copper, cobalt, and nickel selenites: Synthetic analogs of chalcomenite, cobaltomenite, and ahlfeldite, *Spect. Let.* **50** (2017) 539-544.
7. R. L. Frost and E. C. Keeffe, Raman spectroscopic study of the selenite minerals – chalcomenite $CuSeO_3 \cdot 2H_2O$, clinochalcomenite and cobaltomenite, *J. Raman Spectrosc.* **39** (2008) 1789–1793.
8. V. G. Krivovichev, M. V. Charykova, and A. V. Vishnevsky, The thermodynamics of selenium minerals in near-surface environments, *Minerals* **7** (2017) 188.
9. M. V. Charykova, M. I. Lelet, V. G. Krivovichev, N. M. Ivanova, and E. V. Suleimanov, A calorimetric and thermodynamic investigation of the synthetic analogue of chalcomenite, $CuSeO_3 \cdot 2H_2O$, *Eur. Journal Miner.* **29** (2017) 269-277.
10. D. Errandonea and J. Ruiz-Fuertes, A brief review of the effects of pressure on wolframite-type oxides, *Crystals* **8** (2018) 71.

11. O. Grasset, C. Sotin, O. Mousis, and M. Loic, High Pressure Experiments in the System $MgSO_4$-H_2O: Implications for Europa, *Lunar Planet Sci Conf* **31** (2000) 1386.
12. J.M. Meusburger, M. Ende, D. Talla, M. Wildner, and R. Miletich, Transformation mechanism of the pressure-induced C2/c-to-P1 transition in ferrous sulfate monohydrate single crystals, *J. Sol. State Chem.* **277** (2019) 240–252.
13. J. Gonzalez-Platas, A. Muñoz, P. Rodríguez-Hernández, and Daniel Errandonea, High-pressure single-crystal X-ray diffraction of lead chromate: Structural determination and reinterpretation of electronic and vibrational properties, *Inorg. Chem.* **58** (2019) 5966-5979.
14. T. Degen, M. Sadki, E. Bron, U. Konig, G. Nénert, The HighScore suite, *Powder diffraction* **29** (2014) S13-S18.
15. Rigaku Oxford Diffraction, 2016, CrysAlisPro Software system, version 1.171.40.53, Rigaku Corporation, Oxford, UK.
16. R. J. Angel, Absorption corrections for diamond-anvil pressure cells implemented in the software package Absorb6.0, *J. Appl. Crystallogr.* **37** (2004) 486-492.
17. R. J. Angel, M. Bujak, J. Zhao, G. D. Gatta, and S. D. Jacobsen, Effective hydrostatic limits of pressure media for high-pressure crystallographic studies, *J. Appl. Crystallogr.* **40** (2007) 26-32.
18. H. K: Mao, J. Xu, and P. M. Bell, Calibration of the ruby pressure gauge to 800 kbar under quasi-hydrostatic conditions, *J. Geophys. Res.* **91** (1986) 4673– 4676.
19. D. Errandonea, A. Muñoz, and J. Gonzalez-Platas, Comment on "High-pressure x-ray diffraction study of YBO_3/Eu^{3+}, $GdBO_3$, and $EuBO_3$: Pressure-induced amorphization in $GdBO_3$", *J. Appl. Phys.* **115** (2014) 216101.
20. G. M. Sheldrick, A short history of SHELX, *Acta Cryst.* **A64** (2008) 112-122.
21. G. Kresse and J. Furthmuller, Efficient iterative schemes for ab initio total-energy calculations using a plane-wave basis set, *J. Phys. Rev. B* **54** (1996) 11169–11186.
22. G. Kresse and D. Joubert, From ultrasoft pseudopotentials to the projector augmented-wave method, *Phys. Rev. B* **59** (1999) 1758-1775.
23. J. P. Perdew, A. Ruzsinszky, G. I. Csonka, O. A. Vydrow, G. E. Scuseria, L. A. Constantin, X. Zhou, and K. Burke, Restoring the Density-Gradient Expansion for Exchange in Solids and Surfaces. *Phys. Rev. Lett.* **100** (2008) 136406.
24. M. Dion, H. Rydberg, E. Schröder, D. C. Langreth, and B. I. Lundqvist, Van der Waals density functional for general geometries, *Phys. Rev. Lett.* **92** (2004) 246401.
25. H. J. Monkhorst and J. D. Pack, Special points for Brillouin-zone integrations, *Phys. Rev. B* **13** (1976) 5188 - 5192.
26. A. Mujica, A. Rubio, A.; Muñoz, and R. J. Needs, High-pressure phases of group-IV, III–V, and II–VI compounds, Rev. Mod. Phys. 75 (2003) 863 – 912.
27. K. Parlinski, Computer code PHONON, http://wolf.ifj.edu.pl/phonon/.
28. C. Cazorla, D. Errandonea, and E. Sola, High-pressure phases, vibrational properties, and electronic structure of $Ne(He)_2$ and $Ar(He)_2$: A first-principles study, *Phys. Rev. B* **80** (2009) 064105.
29. D. Errandonea, D. Santamaria-Perez, S. N. Achary, and A. K. Tyagi, P Experimental evidence for pressure-driven isostructural and symmetry-breaking phase transitions on $Bi_{14}CrO_{24}$, *Solid State Commun.* **182** (2014) 50-54.
30. D. Errandonea, Landau theory applied to phase transitions in calcium orthotungstate and isostructural compounds, *EPL* **77** (2007) 56001.
31. D. Errandonea, A. Muñoz, P. Rodríguez-Hernández, J. E. Proctor, F. Sapiña, and M. Bettinelli, Theoretical and experimental study of the crystal structures, lattice vibrations, and band structures of monazite-type $PbCrO_4$, $PbSeO_4$, $SrCrO_4$, and $SrSeO_4$, *Inorg. Chem.* **54** (2015) 7524-7535.
32. S. López-Moreno, D. Errandonea, P. Rodríguez-Hernández, and A. Muñoz, Polymorphs of $CaSeO_4$ under pressure: A first-principles study of structural, electronic, and vibrational properties, *Inorg. Chem.* **54** (2015) 1765-1777.
33. F. Birch, Finite elastic strain of cubic crystals, *Phys. Rev.* **71** (1947) 809-824.
34. J. Gonzalez-Platas, M. Alvaro, F. Nestola, and R. J. Angel, EosFit7-GUI: A new GUI tool for equation of state calculations, analyses. and teaching, *Journal of Applied Crystallography* **49** (2016) 1377-1382.
35. A. D. Fortes, K. S. Knight, and I. G. Wood, Structure, thermal expansion and incompressibility of $MgSO_4{\cdot}9H_2O$, its relationship to meridianiite ($MgSO_4{\cdot}11H_2O$) and possible natural occurrences, *Acta Cryst. B* **73** (2017) 47-64.

36. J. Fu and W. Lin, Elastic constants and homogenized moduli of gypsum structure based on density functional theory, *Advances in Engineering Research* **120** (2018) 390–395.
37. E. Bandiello, D. Errandonea, S. Ferrari, J. Pellicer-Porres, D. Martínez-García, S. N. Achary, A. K. Tyagi, and C. Popescu, Pressure-Induced Hexagonal to Monoclinic Phase Transition of Partially Hydrated $CePO_4$, *Inorg. Chem.* **58** (2019) 4480-4490.
38. D. J. Frost, The stability of dense hydrous magnesium silicates in Earth's transition zone and lower mantle, *Mantle Petrology: Field Observations and High Pressure Experimentation* 6 (1999) 283-296.
39. L. Gracia, A. Beltrán, D. Errandonea, and J. Andrés, $CaSO_4$ and its pressure-induced phase transitions: A density functional theory study, *Inorg. Chem.* **51** (2012) 1751-1759.
40. A. Benmakhlouf, D. Errandonea, M. Bouchenafa, S. Maabed, A. Bouhemadoud, and A. Bentabete, New pressure-induced polymorphic transitions of anhydrous magnesium sulfate, *Dalton Trans.* **46** (2017) 5058-5068
41. See The Materials Project; https://materialsproject.org/materials/mp-22414/
42. H. Effenberg, Verfeinerung der Kristall struktur von syntetischem Teinem $CuTeO_3{\cdot}2H_2O$, *Tschermaks Minelarogische und Petrologische Mittelungen* **24** (1977) 287.
43. V. F. Gladkova and Y. D. Kondrashev, Cyrstal structure of $ZnSeO_3{\cdot}2H_2O$, *Soviet Physics Crystallography* **9** (1964) 149.
44. K. Sathianandan, L. D. McCory, and J. L. Margrave, Infrared absorption spectra of inorganic solids—III Selenates and selenites, *Spectrochim. Acta* **20** (1964) 957-963.
45. V. N. Makatun, V. V. Pechkovskii, R. Y. Mel'nikova, and S. S. Gusev, Infrared spectra of copper selenites, *Zhur. Prikl. Spektrosk.* **12** (1970) 497-503.
46. D. Errandonea, J. Pellicer-Porres, M. C. Pujol, J. J. Carvajal, and M. Aguiló, Room-temperature vibrational properties of potassium gadolinium double tungstate under compression up to 32 GPa, *J. Alloys Compd.* **638** (2015) 14–20.
47. M. T. Dove, Theory of displacive phase transitions in minerals, *Am. Mineral.* **82** (1997) 213–244.
48. D. Santamaria-Perez, D. Errandonea, P. Rodriguez-Hernandez, A. Muñoz, R. Lacomba-Perales, A. Polian, and Y. Meng, Polymorphism in strontium tungstate $SrWO_4$ under quasi-hydrostatic compression, *Inorg. Chem.* **55** (2016) 10406.